Frontiers of Information Technology & Electronic Engineering
www.zju.edu.cn/jzus; engineering.cae.cn; www.springerlink.com
ISSN 2095-9184 (print); ISSN 2095-9230 (online)
E-mail: jzus@zju.edu.cn

A combined modulated feedback and temperature compensation approach to improve bias drift of a closed-loop MEMS capacitive accelerometer

Ming-jun MA[†], Zhong-he JIN[†‡], Hui-jie ZHU

(*Micro-Satellite Research Center, Zhejiang University, Hangzhou 310027, China*)

[†]E-mail: edward-ma@zju.edu.cn; jinzh@zju.edu.cn

Received Oct. 25, 2014; Revision accepted Apr. 14, 2015; Crosschecked May 4, 2015

Abstract: The bias drift of a micro-electro-mechanical systems (MEMS) accelerometer suffers from the 1/*f* noise and the temperature effect. For massive applications, the bias drift urgently needs to be improved. Conventional methods often cannot address the 1/*f* noise and temperature effect in one architecture. In this paper, a combined approach on closed-loop architecture modification is proposed to minimize the bias drift. The modulated feedback approach is used to isolate the 1/*f* noise that exists in the conventional direct feedback approach. Then a common mode signal is created and added into the closed loop on the basis of modulated feedback architecture, to compensate for the temperature drift. With the combined approach, the bias instability is improved to less than 13 μ*g*, and the drift of the Allan variance result is reduced to 17 μ*g* at 100 s of the integration time. The temperature coefficient is reduced from 4.68 to 0.1 mg/°C. The combined approach could be useful for many other closed-loop accelerometers.

Key words: Bias drift, Closed-loop MEMS accelerometer, Modulated feedback approach, Temperature compensation
doi:10.1631/FITEE.1400349 **Document code:** A **CLC number:** TN43

1 Introduction

The drift of MEMS inertial sensors has been investigated for a long time. The drift can be due to multiple reasons such as noise, temperature variation, environmental vibrations, electronic reference drift, and humidity changes. Noise and temperature variation are usually considered as the major reasons for the drift (Prikhodko *et al.*, 2013). Allan variance (Allan, 1966; IEEE, 1998) is a powerful method for characterizing drift, in which different piecewise fitted lines correspond to different noise terms. The fitted line at a slope of 0 is defined as the bias instability for inertial sensors. The bias instability is caused mainly by 1/*f* noise. The common methods of canceling 1/*f* noise are correlated double sampling (CDS) and chopper stabilization (CHS) (Enz and Temes, 1996; Wongkomet and Boser, 1998; Kajita *et al.*, 2002; Wu *et al.*, 2004; Dong *et al.*, 2010). CDS is often implemented in discrete time, while CHS can be operated in continuous time. For inertial sensors, CDS can be compatible with discrete-time architecture like the Sigma-Delta interface (Amini *et al.*, 2006; Dong *et al.*, 2007). However, for continuous-time operation, it is necessary to exploit an effective approach like CHS (Li and Horsley, 2014).

On the other hand, long-term drift is concerned in many applications. It is often caused by temperature effects. A variety of temperature compensation methods have been investigated. Some researchers designed low temperature dependence interface circuits (Ko and Cho, 2010), or applied a complicated algorithm to reduce the temperature drift (Lee and Rhim, 2012). Doping is used for temperature

‡ Corresponding author
ORCID: Ming-jun MA, http://orcid.org/0000-0002-2012-8699

compensation (Samarao and Ayazi, 2012) with careful design of the fabrication process such that the devices obtain a low temperature coefficient. Active heating by an integrated heater is also used (Lee *et al.*, 2003; Lakdawala and Fedder, 2004) so that the temperature is kept almost constant.

Different from these methods which concern only 1/*f* noise or temperature and are usually incompatible for dealing with the very two terms in one architecture, a combined approach is proposed to address the bias drift in a continuous-time closed-loop MEMS accelerometer. A modulated feedback approach is used to isolate the 1/*f* noise. The bias instability is improved to 8 μg as a consequence. Then a common mode signal added to the closed loop is adopted to minimize the long-term temperature effects of the closed-loop MEMS accelerometer. The temperature coefficient is reduced to 0.1 mg/°C with first-order linear compensation. The drift of the Allan variance is reduced to 17 μg at 100 s of the integration time. This combined approach exploits the potentials of the closed loop and can be used for many other MEMS accelerometers.

2 Methods

2.1 Accelerometer structure and fabrication

The main theme of this paper is focused on offering a universal method to improve the bias drift. Therefore, the accelerometer here is designed to contain a simple structure and fabrication process in order to be easily fabricated. As illustrated in Fig. 1, the accelerometer has four U-shaped beams to support the proof mass at the center position. The U-shaped beams also connect the out frame. The silicon layer and glass layer are anodically bonded together. There are two types of electrode sputtered on the glass: one is the electrode for sensing, and the other is the electrode for feedback operation. Under such a configuration, the accelerometer employs the area-variable capacitor.

The fabrication process employs the silicon-on-glass (SOG) structure with five photo masks. Fig. 2 shows the fabrication process of the accelerometer with U-shaped beam. A detailed process can be referred to Zheng *et al.* (2009).

The designed basic mechanical and electrical parameters of the accelerometer and the measured resonant frequency are listed in Table 1 for clear display. According to the area-variable capacitor structure, the accelerometer has a Brownian noise as small as 0.02 μg/(Hz)$^{1/2}$ under atmospheric conditions.

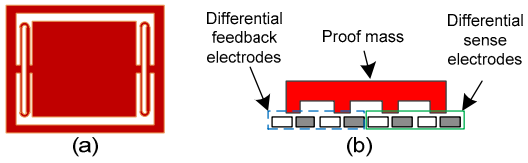

Fig. 1 Mechanical and electrical structures of the accelerometer

(a) Mechanical structure with U-shaped beams; (b) Two types of variable capacitors underneath the proof mass, one used for feedback and the other for sensing

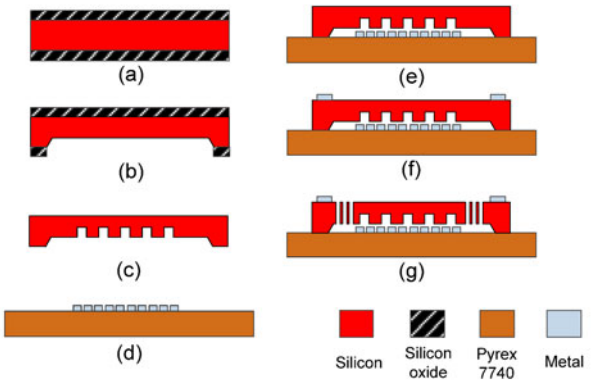

Fig. 2 Fabrication process of the accelerometer with U-shaped beam

A 250 μm N type silicon wafer is first oxidized on both sides in (a), and then a 2.5 μm gap is created by using potassium hydroxide (KOH) to etch the backside of the silicon wafer in (b). A series of grooves are etched further to form the silicon electrodes at the backside of the silicon wafer using a deep reactive-ion etching (DRIE) process in (c). The metal electrodes are sputtered on the frontside of glass Pyrex 7740 and then etched in (d). The silicon wafer backside and the frontside of glass are anodically bonded together in (e), in which the etched silicon electrodes and metal electrodes have overlapping areas to form the variable capacitors. Two types of variable capacitors, i.e., the differential sense capacitors and the differential feedback capacitors, are created meanwhile. After anodic bonding, the frontside of the silicon wafer is sputtered with metal and etched to form the metal pads for wiring in (f). Finally, a 250 μm DRIE is employed to release the structure in (g)

This SOG structure has some advantages so that we choose to use it on the accelerometer. First, to achieve a small Brownian noise, slide film damping

and large proof mass are preferred. SOG can meet these two requirements. Second, the parasitic capacitance of the SOG structure is small compared with silicon-on-insulator (SOI) or other similar structures, thus guaranteeing better noise performance (Chae *et al.*, 2005). Third, the bonding temperature is low and the thermal expansion coefficient of glass Pyrex 7740 is often a good match to that of silicon.

Table 1 Specifications of the accelerometer

Parameter	Value
Mass	~3 mg
Resonant frequency	~800 Hz
Initial capacitance	6.5 pF
Capacitance gap	1.5 μm
Capacitive sensitivity	~0.1 pF/g
Brownian noise	0.02 μg/(Hz)$^{1/2}$
Capacitor gap	1.5 μm
U-shaped beam length	951 μm
U-shaped beam width	15 μm
Center radius of U-shaped beam	20 μm
Thickness	250 μm

Note that there is still a residual thermal expansion mismatch for the glass and silicon, which may induce the bias drift. Such an issue can be solved by the temperature compensation technique. Creating a symmetric structure to nullify the thermal expansion coefficient difference can be another solution.

2.2 Introduction to closed loop with a direct feedback approach

Much of the literature has reported the closed-loop diagram (Josselin *et al.*, 1999; Amini *et al.*, 2006; Aaltonen and Halonen, 2009). Typically, their feedback approaches consist of feedback voltage which has the same frequency as the input acceleration. So, the input inertial force can be nullified by the electrostatic feedback force generated from the feedback voltage. Such an approach is named the direct feedback approach (DFA) in this paper. Since the bandwidth of the closed-loop accelerometer is often less than 1 kHz, the feedback voltage has the same frequency lower than 1 kHz, where there exists the 1/f noise. Then the 1/f noise stemming from feedback voltage will inevitably affect the performance of the accelerometer.

To be specific, a closed-loop diagram with DFA is presented in Fig. 3. Note that such an accelerometer is not a resonant accelerometer. The carrier wave with frequency ω_c modulates the differential changes of sense capacitors caused by acceleration, and is detected by the capacitance-to-voltage (C/V) block. This is the traditional chopper stabilization to sense the signal. Such a signal is fed to the A/D module, and is synchronically demodulated in the digital domain. The signal at the output of demodulation has the same frequency as the input acceleration. This signal is then sent to the proportional-integral-derivative (PID) controller and the voltage V_{fb} is formed at the PID output. A bias voltage V_{bias} is created and the differential feedback voltage $V_{fb}\pm V_{bias}$ is generated and sent to the differential feedback electrodes respectively. The net electrostatic feedback force can nullify the inertial force. This is the operation of the closed loop.

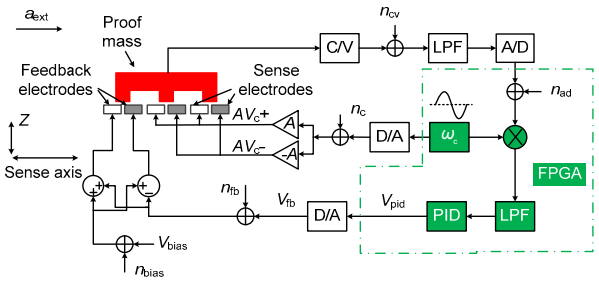

Fig. 3 Diagram of a closed-loop MEMS accelerometer with a direct feedback approach

Note that we choose the continuous-time closed loop over the Sigma-Delta loop because the loop stability criteria of the Sigma-Delta structure are more sophisticated, especially for the higher-order Sigma-Delta structure which enables better noise shaping. There is no precise analytic approach to deciding the stability of a modulator without resorting to simulation (Schreier, 1993; Dong *et al.*, 2007). This means that the loop stability will be frequently examined when the loop parameters are changed, whereas the PID controller in a continuous-time closed loop can stabilize a large scale of loop parameters, and we are able to focus on noise performance and temperature drift analysis. Also, the 1-bit feedback form of the Sigma-Delta structure has problems such as tonal behavior and limited cycles, which will degrade the performance (Dong *et al.*, 2007). In addition, many high-precision accelerometers have

adopted this continuous-time closed-loop form (Willemenot and Touboul, 2000; Yoshida *et al.*, 2005). Due to these considerations the continuous-time closed-loop will be a good choice.

According to the closed-loop form, several noise sources are labeled in Fig. 3. Typically, for the accelerometer with a large proof mass and large nominal capacitance, as shown in Fig. 2, the electronic noise dominates in closed-loop MEMS capacitive accelerometer output, whereas the Brownian noise is usually negligible. The electronic noises come from the analog circuit and the A/D and D/A modules. The additive noises n_c, n_{cv}, and n_{ad} are the white noises at frequency around ω_c, while noises n_{fb} and n_{bias} should be modeled as low-frequency noise as $1/f$ noise, since V_{bias} is the bias DC voltage and V_{fb} is the low-frequency voltage. Under such a premise, the $1/f$ noise in the feedback path may deteriorate the overall closed-loop performance, as confirmed by Josselin *et al.* (1999) and Aaltonen and Halonen (2009). When V_{fb}, V_{bias} and their noises n_{fb}, n_{bias} are known, the net electrostatic feedback force $F_{e,x}$ can be written as

$$F_{e,x}=\frac{1}{2}\frac{\partial C}{\partial x}\left\{[(V_{bias}+n_{bias})+(V_{fb}+n_{fb})]^2 -[(V_{bias}+n_{bias})-(V_{fb}+n_{fb})]^2\right\}. \tag{1}$$

The fully expanded Eq. (1) is written as

$$F_{e,x}=\frac{1}{2}\frac{\partial C}{\partial x}\Big[V_{bias}^2+n_{bias}^2+2V_{bias}n_{bias}+V_{fb}^2+n_{fb}^2+2V_{fb}n_{fb} -V_{bias}^2-n_{bias}^2-2V_{bias}n_{bias}-V_{fb}^2-n_{fb}^2-2V_{fb}n_{fb} +4(V_{bias}+n_{bias})(V_{fb}+n_{fb})\Big]. \tag{2}$$

Considering the mathematical meaning of Eq. (2), most of the terms in Eq. (2) are nullified. The simplification of Eq. (2) yields

$$F_{e,x}=2\frac{\partial C}{\partial x}(V_{bias}V_{fb}+V_{bias}n_{fb}+V_{fb}n_{bias}+n_{bias}n_{fb}). \tag{3}$$

$F_{e,x}$ contains the $1/f$ noise from n_{bias} and n_{fb} as a consequence, and then the accelerometer will suffer from such $1/f$ noise since $F_{e,x}$ is directly exerted on the accelerometer. At low frequencies, $1/f$ noise dominates the closed-loop output spectrum and can deteriorate the low-frequency performance. Therefore, it is necessary to minimize the $1/f$ noise in the feedback path.

Apart from the $1/f$ noise in the feedback path, there is $1/f$ noise existing in the forward path, usually from the pick-off circuit, or the C/V circuit in Fig. 3. Since the C/V circuit employs the chopper stabilization technique, the $1/f$ noise from the amplifier can be ignored (Petkov and Boser, 2004). Theoretical analysis believes that the $1/f$ noise in the forward path is quite small compared to the $1/f$ noise in the feedback path.

2.3 Modulated feedback approach

Correlated double sampling (CDS) and chopper stabilization (CHS) techniques are the widely used approaches to addressing the offset and its accompanied $1/f$ noise. The former requires strict timing of the switch capacitors such that it is not applicable for continuous-time applications. The latter incorporates the concept of modulation and demodulation, which can be easily realized under the continuous-time closed-loop accelerometer structure.

The common usage of CHS nowadays is focused on minimizing the low-frequency noises in the pick-off circuit, i.e., the C/V circuit in this study. Different from conventional CHS techniques, the modulated feedback approach (MFA) aims to deal with the low-frequency noise in feedback circuit. Also, different from the linear multiplier or chopper used by traditional CHS techniques (Petkov and Boser, 2004), MFA uses the voltage-to-force process of variable capacitors in the feedback path to realize the demodulation, and the additional demodulator is saved. Such a method was previously adopted by Cui *et al*. (2011) to minimize the electrical coupling of the gyroscope. Moreover, we will show later on that the adoption of MFA can derive another temperature compensation scheme.

MFA simply modulates the previous V_{bias} and V_{fb} signals on another carrier wave at frequency ω_d, which is different from ω_c. The signals V_{bias} and V_{fb} are changed into $V_{bias\_\omega d}$ and $V_{fb\_\omega d}$ respectively, with white noises near frequency ω_d as $n_{fb\_\omega d}$ and $n_{bias\_\omega d}$ respectively:

$$V_{bias\_\omega d}=V_{bias0}\cos(\omega_d t+\theta)+n_{bias\_\omega d}, \tag{4}$$

$$V_{fb\_\omega d}=V_{pid}\cos(\omega_d t+\varphi)+n_{fb\_\omega d}, \tag{5}$$

where V_{bias0} is the amplitude of $V_{\text{bias\_}\omega\text{d}}$, with value equal to that of previous V_{bias}, and V_{pid} is the previous PID output. The voltage-to-force process of the variable capacitor can automatically demodulate the signal, which has been modulated on the carrier at frequency ω_{d}. By substituting Eqs. (4) and (5) into Eq. (3), the electrostatic feedback force $F_{\text{e},x\_\omega\text{d}}$ is yielded as

$$F_{\text{e},x\_\omega\text{d}} = 2\frac{\partial C}{\partial x}\{V_{\text{bias0}}V_{\text{pid}}/2\cdot[\cos(\theta-\varphi)+\cos(2\omega_{\text{d}}t+\theta+\varphi)]+V_{\text{bias0}}\cos(\omega_{\text{d}}t+\theta)n_{\text{fb\_}\omega\text{d}}+V_{\text{pid}}\cos(\omega_{\text{d}}t+\varphi)n_{\text{bias\_}\omega\text{d}}+n_{\text{bias\_}\omega\text{d}}n_{\text{fb\_}\omega\text{d}}\}, \quad (6)$$

where θ and φ are the modulated phases of the two signals, respectively. The modulated signals $V_{\text{pid}}\cos(\omega_{\text{d}}+\theta)$ and $V_{\text{bias0}}\cos(\omega_{\text{d}}+\varphi)$ have already been demodulated in Eq. (6). The part $(\partial C/\partial x)V_{\text{bias0}}V_{\text{pid}}\cos(\theta-\varphi)$ in Eq. (6) is the very electrostatic force to nullify the inertial force, while other parts at frequencies ω_{d} and $2\omega_{\text{d}}$ are filtered by the mechanical element of the accelerometer.

Fig. 4 presents a detailed explanation on noises and the implementation of MFA. The previous $1/f$ noises n_{fb} and n_{bias}, and the white noises $n_{\text{fb\_}\omega\text{d}}$ and $n_{\text{bias\_}\omega\text{d}}$ near frequency ω_{d}, are all added to the output of the D/A module. If V_{pid} and V_{bias0} are modulated before D/A in the digital domain, n_{fb} and n_{bias} can be isolated after the high-pass filter. Then the dominant noises that V_{pid} and V_{bias0} carry are the white noises near frequency ω_{d}, i.e., $n_{\text{fb\_}\omega\text{d}}$ and $n_{\text{bias\_}\omega\text{d}}$.

As for the implementation, only an additional D/A module, a signal synthesizer in FPGA, and first-order resistor-capacitor (RC) high-pass filters are added to the original interface circuits. The RC high-pass filters are used to remove the $1/f$ noise generated in the feedback path.

2.4 Novel temperature compensation based on a modulated feedback approach

The improvement of bias drift not only relies on the reduction of $1/f$ noise, but also depends on the alleviation of environmental effects on the accelerometer. Under the ambient condition without temperature control, the temperature effect on the drift is more noticeable than $1/f$ noise. An effective temperature compensation scheme would undoubtedly improve the drift performance and render the accelerometer more immune to a harsh environment.

We hope to treat the temperature drift by one approach without fabricating a thermometer or using temperature controller to control the environmental temperature. Hence, a signal in the closed loop that can represent the temperature variation is desirable. The proposed novel temperature approach is built on the basis of the MFA structure, and it derives such a signal which can represent the temperature variation.

The operation of the novel temperature compensation is illustrated as follows: A new carrier wave at frequency ω_{com} is generated in the digital domain. This signal is added to the modulated signal $V_{\text{bias\_}\omega\text{d}}$, and these two signals are outputted by the same D/A module, as depicted in Fig. 5. The

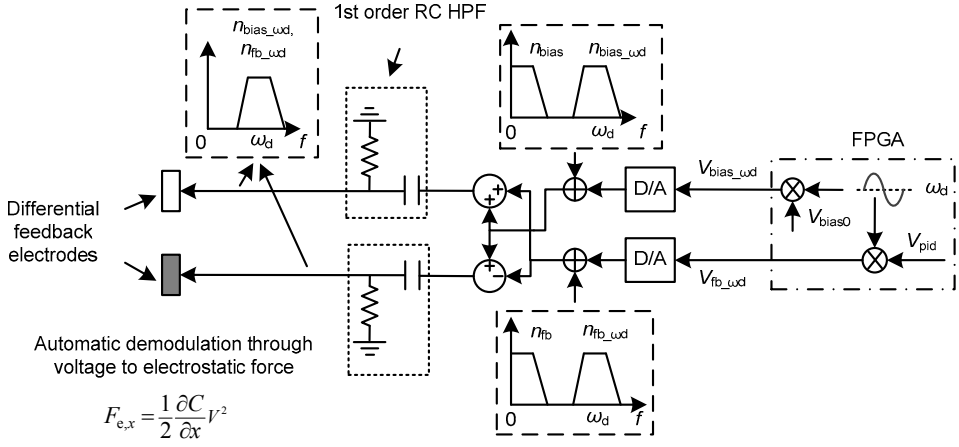

Fig. 4 Schematic of the noise spectrum in a modulated feedback approach and implementation of the modulated feedback approach

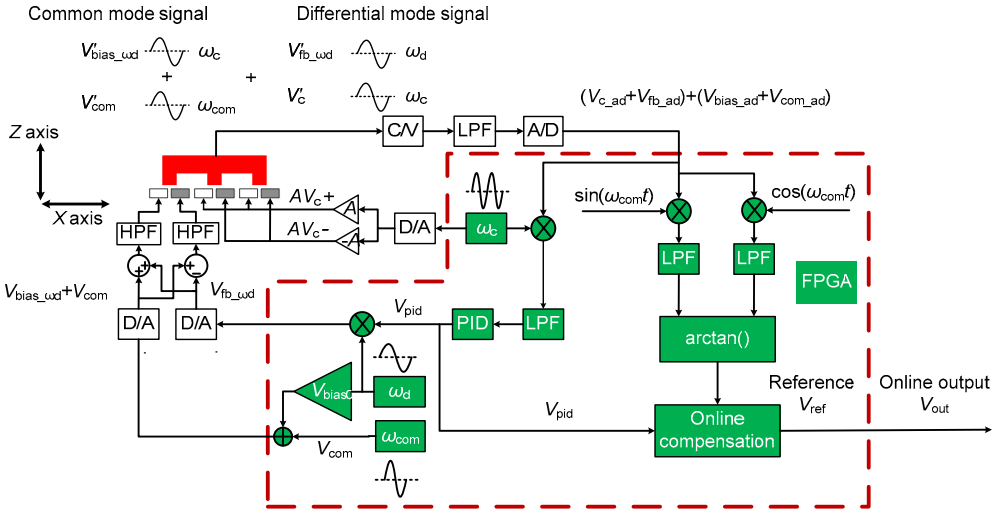

Fig. 5 Novel closed-loop diagram with a modulated feedback approach and temperature compensation

previous differential feedback voltage $V_{\text{bias\_}\omega\text{d}}\pm V_{\text{fb\_}\omega\text{d}}$ now becomes $(V_{\text{bias\_}\omega\text{d}}+V_{\text{com}})\pm V_{\text{fb\_}\omega\text{d}}$. $V_{\text{bias\_}\omega\text{d}}$ and V_{com} are the common mode voltages as for the differential feedback capacitors. These two signals modulate the sum of differential feedback capacitors and are sensed by the C/V block, while $V_{\text{fb\_}\omega\text{d}}$ and V_{c} are the differential mode voltages. The two signals modulate the changes of differential feedback capacitors and differential sense capacitors. Therefore, as shown in Fig. 5, there are four signals at the output of the C/V block, and they are all sent to the A/D module. The signals at the input of the A/D module can be represented as follows:

$$V_{\text{ad}}=(V_{\text{c\_ad}}+V_{\text{fb\_ad}})+(V_{\text{bias\_ad}}+V_{\text{com\_ad}}). \quad (7)$$

Specifically, $V_{\text{c\_ad}}$ is the carrier wave at frequency ω_{c} to modulate the differences of differential sense capacitance; $V_{\text{fb\_ad}}$ is the carrier wave at frequency ω_{d} to modulate the differences of differential feedback capacitors. They are all the differential mode signals. $V_{\text{bias\_ad}}$ is the carrier wave at frequency ω_{d} to modulate the sum of differential feedback capacitors. $V_{\text{com\_ad}}$ is the carrier wave at frequency ω_{com} to modulate the sum of differential feedback capacitors. These two signals are the common mode signals. The differential mode signals and the common mode signals have such expressions as

$$V_{\text{c\_ad}}=V_{\text{c}}(C_{\text{SL}}-C_{\text{SR}})G_{\text{cv}}(\omega_{\text{c}}), \quad (8)$$
$$V_{\text{fb\_ad}}=V_{\text{fb\_}\omega\text{d}}(C_{\text{FL}}-C_{\text{FR}})G_{\text{cv}}(\omega_{\text{d}}), \quad (9)$$
$$V_{\text{bias\_ad}}=V_{\text{bias\_}\omega\text{d}}(C_{\text{FL}}+C_{\text{FR}})G_{\text{cv}}(\omega_{\text{d}}), \quad (10)$$
$$V_{\text{com\_ad}}=V_{\text{com}}(C_{\text{FL}}+C_{\text{FR}})G_{\text{cv}}(\omega_{\text{com}}), \quad (11)$$

where C_{SL} and C_{SR} are the differential sense capacitors, C_{FL} and C_{FR} the differential feedback capacitors, and $G_{\text{cv}}(\omega_{\text{c}})$, $G_{\text{cv}}(\omega_{\text{d}})$, and $G_{\text{cv}}(\omega_{\text{com}})$ the C/V module transfer functions at frequencies ω_{c}, ω_{d}, and ω_{com}, respectively.

Note that $C_{\text{FL}}-C_{\text{FR}}$ and $C_{\text{SL}}-C_{\text{SR}}$ are caused by input acceleration, i.e., $C_{\text{FL}}-C_{\text{FR}}$ and $C_{\text{SL}}-C_{\text{SR}}$ contain the acceleration information, while $C_{\text{FL}}+C_{\text{FR}}$ is the sum of differential feedback capacitors and the acceleration information does not exist. This can be seen from Eqs. (12) and (13):

$$C_{\text{FL}}=C_{\text{F0}}+\Delta C,\quad C_{\text{FR}}=C_{\text{F0}}-\Delta C, \quad (12)$$
$$C_{\text{FL}}-C_{\text{FR}}=2\Delta C,\quad C_{\text{FL}}+C_{\text{FR}}=2C_{\text{F0}}, \quad (13)$$

where C_{F0} is the initial feedback capacitance, and ΔC is the capacitance change caused by input acceleration. Hence, $C_{\text{FL}}+C_{\text{FR}}$ has no relation with acceleration, and the variation of $V_{\text{com\_ad}}$ is insensitive to input acceleration.

Actually, the common mode voltage V_{com} is driving the accelerometer along the z-axis, and the gap of the capacitor is vibrating. This force is different from the electrostatic feedback force $F_{\text{e},x\_\omega\text{d}}$ which is generated along the x-axis. The equation of $V_{\text{com\_ad}}$ is further modified as

$$V_{\text{com\_ad}}=\frac{V_{\text{com}}2C_{\text{F0}}G_{\text{cv}}(\omega_{\text{com}})}{1+z/d_0}, \quad (14)$$

$$m\ddot{z}+c\dot{z}+k_z z=F_{\text{com}}, \tag{15}$$

$$\begin{aligned}F_{\text{com}}&=\frac{1}{2}\frac{\partial(2C_{\text{F0}})}{\partial z}[V_{\text{com0}}\sin(\omega_{\text{com}}t)]^2\\&=\frac{1}{2}\frac{\partial C_{\text{F0}}}{\partial z}V_{\text{com0}}^2[1-\cos(2\omega_{\text{com}}t)],\end{aligned} \tag{16}$$

where z is the change of the capacitance gap induced by V_{com}, d_0 is the initial gap of capacitors, V_{com0} is the amplitude of V_{com}, F_{com} is the electrostatic force at the z-axis induced by V_{com}, and F_{com} has a DC part and a second harmonic frequency part. Substituting Eq. (16) into Eq. (15) yields the solution of z:

$$z=z_0+d\sin(2\omega_{\text{com}}t+\phi), \tag{17}$$

$$z_0=\frac{1}{2}\frac{\partial C_{\text{F0}}}{\partial z}\frac{V_{\text{com0}}^2}{k_z}, \tag{18}$$

$$d=\frac{z_0k_z}{m\sqrt{(\omega_z^2-4\omega_{\text{com}}^2)^2+(2\omega_z\omega_{\text{com}}/Q_z)^2}}, \tag{19}$$

$$\phi=-\arctan\left(\frac{2\omega_z\omega_{\text{com}}}{Q_z(\omega_z^2-4\omega_{\text{com}}^2)}\right), \tag{20}$$

$$\omega_z=\sqrt{k_z/m}, \tag{21}$$

$$Q_z=m\omega_z/c, \tag{22}$$

where ω_z is the resonant frequency of the accelerometer at the z-axis, Q_z is the quality factor at the z-axis, z_0 is the DC bias of displacement at the z-axis, d is the vibrating amplitude of z, and ϕ is the phase of displacement z. However, since the spring stiffness k_z of the z-axis is rather large, in the case of this accelerometer around 3000 N/m, a V_{com} of 0.1 V at 8 kHz would result in z_0 and d less than 3 pm along the z-axis, which could be ignored. Hence, by substituting Eq. (17) into Eq. (14), a linearization of the equation with a small range of z can derive

$$\begin{aligned}V_{\text{com\_ad}}=V_{\text{com0}}2C_{\text{F0}}G_{\text{cv}}(\omega_{\text{com}})\frac{1}{1+z_0/d_0}\cdot\Bigg[&\sin(\omega_{\text{com}}t)\\&-\frac{1}{1+z_0/d_0}\left(\frac{d}{2d_0}\sin(\omega_{\text{com}}t+\phi)+\frac{d}{2d_0}\sin(3\omega_{\text{com}}t+\phi)\right)\Bigg].\end{aligned} \tag{23}$$

The signal $V_{\text{com\_ad}}$ is then sent to the A/D module, and demodulated by the in-phase and quadrature (IQ) demodulation process, as depicted in Fig. 5. The frequency ω_{com} of $V_{\text{com\_ad}}$ is demodulated to the baseband; the frequency $3\omega_{\text{com}}$ is demodulated to be $2\omega_{\text{com}}$ and $4\omega_{\text{com}}$, and they are both filtered by the low-pass filter. The final phase extracted by an arctan module in Fig. 5 is simplified as

$$\begin{aligned}\psi=\arctan\Bigg\{&\frac{z_0}{2m(d_0+z_0)}\\&\cdot\frac{2k_z\omega_z\omega_{\text{com}}}{Q_z[(\omega_z^2-4\omega_{\text{com}}^2)^2+(2\omega_z\omega_{\text{com}}/Q_z)^2]}\Bigg\}.\end{aligned} \tag{24}$$

The variation of spring stiffness with temperature T can be written as (Liu *et al.*, 2008)

$$k_z(T)=k_{z0}[1-\alpha(T-T_0)], \tag{25}$$

where α is the spring stiffness temperature coefficient. Then, substituting Eq. (25) into Eq. (21), the linearization result of resonant frequency ω_z is yielded as

$$\omega_z(T)=\omega_{z0}\left[1-\frac{1}{2}\alpha(T-T_0)\right]. \tag{26}$$

Substituting Eq. (26) into Eq. (24), the relationship between phase and temperature is given below:

$$\begin{aligned}\psi(T)=\arctan\Bigg\{&\frac{z_0}{2m(d_0+z_0)}\\&\cdot\frac{2k_z(T)\omega_z(T)\omega_{\text{com}}}{Q_z(T)[(\omega_z(T)^2-4\omega_{\text{com}}^2)^2+(2\omega_z(T)\omega_{\text{com}}/Q_z(T))^2]}\Bigg\}.\end{aligned} \tag{27}$$

With predetermined parameters, the relationship between $\psi(T)$ and temperature T is calculated (Fig. 6). The plot shows that the phase linearly changes with temperature. Hence, we use the phase to indicate the temperature and compensate for the closed-loop output. The phase ψ is also named V_{ref} in Fig. 5.

In addition to the direct relationship between k_z and temperature T in Eq. (25), the temperature may induce the stress for the spring, thus making the stiffness k_z and resonant frequency ω_z change. This is not reflected in Eq. (25). The function of temperature induced stress and the corresponding k_z variation is complicated. Detailed discussions on the stress and

stiffness can be referred to Wortman and Evans (1965) and Karabalin *et al.* (2012). However, in reality, the temperature induced stress will be ultimately reflected in the variation of stiffness k_z. As the phase ψ in Eq. (24) contains parameter k_z, it can also reflect such an influence in the experiments. Such an influence will make the plot of ψ with temperature T not a pure linear relationship.

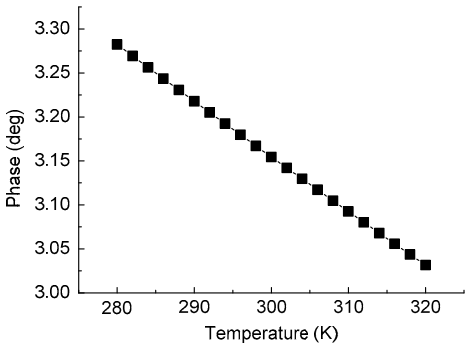

Fig. 6 The calculated relationship between phase ψ and temperature T

2.5 Simulation

The simulation is established by building Simulink models with MFA. The amplitude of V_{bias} in DFA and MFA is adopted as 3 V. Fig. 7 is the transient response to a static 5 m*g* acceleration input. According to Eq. (6), since $\cos(\theta-\varphi)$ is less than 1, the scale factor of the loop with MFA is larger than the loop with DFA. The scale factor of the loop with MFA is 20 V/*g* in simulation.

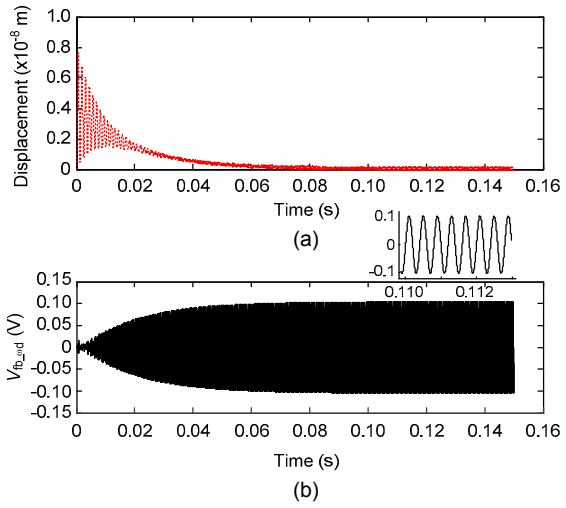

Fig. 7 Transient response to a static 5 m*g* acceleration
(a) Proof mass displacement; (b) Feedback voltage

The simulated spectrum of the output signal is given in Fig. 8. The noise spectrum by using MFA is obviously smaller than that by using DFA. The simulated noise with MFA is around 0.1 μ*g*/(Hz)$^{1/2}$, while the noise with DFA is around 0.6 μ*g*/(Hz)$^{1/2}$ at low frequencies between 10 and 100 Hz.

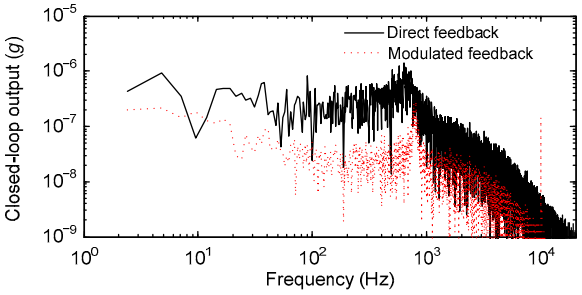

Fig. 8 Simulated spectrum of the PID output with a direct feedback approach and a modulated feedback approach, respectively

3 Experiment results

The experiments are set up in the sequence that the modulated feedback approach is established at first and the temperature compensation architecture constructed then. The frequencies used in the combined approach are listed in Table 2.

Table 2 Frequencies used in closed-loop circuit

Frequency	Value (kHz)
ω_c	150
ω_d	2.5
ω_{com}	8

3.1 Modulated feedback approach experiments

The MFA experiment setup is as presented in Fig. 9. The PCB board with an accelerometer and FPGA are fixed on the rate table, and the signals are generated from the FPGA board and transmitted to the PCB through coaxial wires. The output signals are sampled and sent to the PC using the UART protocol.

The frequency ω_d is chosen to be 2.5 kHz to avoid the resonant frequency of the accelerometer at the *z*-axis, which is located at 4.1 kHz. ω_d also stays away from the 1/*f* noise corner frequency. The time-domain signal $V_{fb\_\omega d}$ after closing the loop is shown

in Fig. 10a, obtained by an Agilent oscilloscope DSO5000A. The settling time of transient response agrees with the simulation result, which is around 30 ms. A smaller wave is observed before the transient response start point. This is due to the incomplete configuration of the parameter transmission from PC to FPGA. The corresponding frequency domain $V_{fb\_\omega d}$ is shown in Figs. 10b and 10c by an HP 89441A vector signal analyzer. Fig. 10b shows $V_{fb\_\omega d}$ at 2.5 kHz and the noise near 2.5 kHz. It can be seen that the noise spectrum is flat in the range of 25−2500 Hz. The closed-loop scale factor is measured to be 18 V/g, giving rise to the noise about 1.8 μg/(Hz)$^{1/2}$ at 5 Hz away from the center frequency 2.5 kHz. Fig. 10c presents the spectrum of signal $V_{fb\_\omega d}$ near 0 Hz to show that there is no significant 1/f noise carried by $V_{fb\_\omega d}$ at frequencies larger than 1 Hz.

The spectrum of digital PID output V_{pid} is sampled and compared between DFA and MFA in Fig. 11. The noise spectrum at low frequencies is distinctly different. The output of MFA is revealed to be smaller than that of DFA, with a difference of more than 20 dB at frequencies lower than 1 Hz, indicating that the impact of 1/f noise in the feedback path on the accelerometer is minimized with MFA.

As to the Allan variance, the open-loop Allan variance is tested at first to show the level of 1/f noise in the forward path. The open-loop output data is sampled for one hour at room temperature. The time-domain trace of the sampled data and its Allan variance result are shown in Fig. 12. The standard deviation (Std) of the time-domain trace is 0.52 mg. The bias instability is 12 μg and the drift is 180 μg in the open-loop mode at 100 s of the integration time. According to this result, it is suspected that the 1/f source in the forward path comes from other paths such as the bias of the proof mass with respect to the ground.

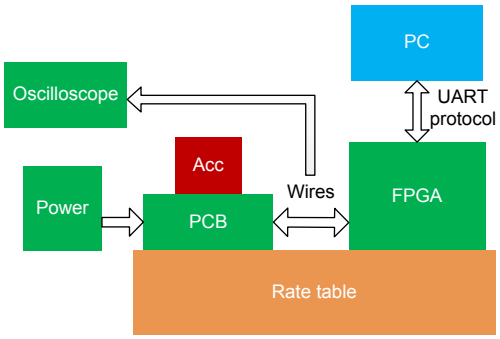

Fig. 9 Schematic of the experiment setup and the connection relationship

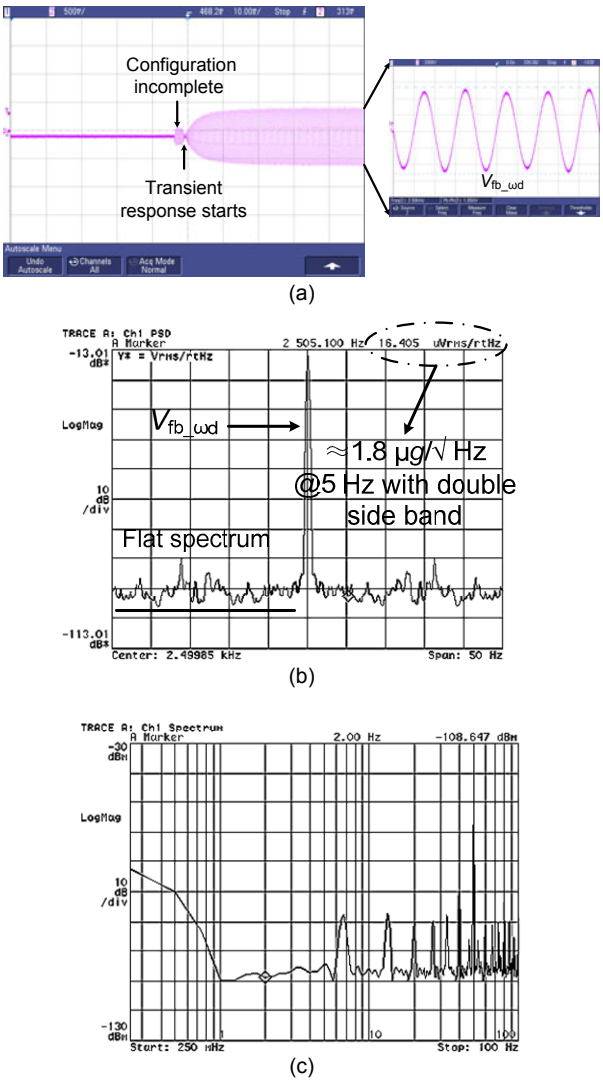

Fig. 10 Signals displayed on the oscilloscope and corresponding spectrum with a modulated feedback approach
(a) $V_{fb\_\omega d}$ displayed on the oscilloscope; (b) $V_{fb\_\omega d}$ signal spectrum near 2.5 kHz (including the noise near ω_d); (c) Noise spectrum of $V_{fb\_\omega d}$ near 0 Hz

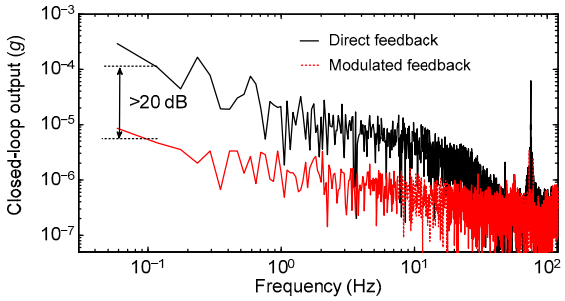

Fig. 11 Measured spectrums of direct and modulated feedback outputs
Both signals are sampled from the digital output of PID blocks

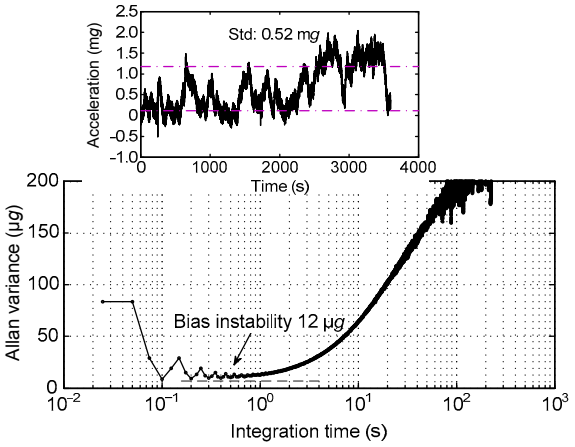

Fig. 12 The open-loop Allan variance results with a zero acceleration input
The inset is the time-domain trace

The closed-loop experiments are conducted to examine the bias drift of the closed-loop output signal V_{pid} with DFA and MFA, respectively. Fig. 13 shows the test results of the closed loop with DFA. The Std of the time-domain trace is 0.35 mg, and the bias instability is 32 μg. The drift is 72 μg at 100 s of the integration time. Compared with the open-loop Allan variance result, the 1/*f* noise in the feedback path is shown to be larger and should be addressed prior to the 1/*f* noise in the forward path.

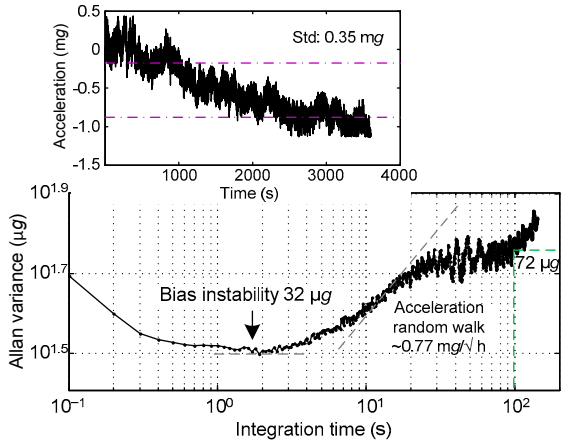

Fig. 13 One-hour stability test with zero acceleration input by applying a direct feedback approach
The large plot shows the Allan variance results and the inset is the time-domain trace

With MFA, the Std is 0.1 mg, and a bias instability of 8 μg is achieved (Fig. 14). The drift is also improved from 72 to 32 μg at 100 s of the integration time, showing that the long-term drift is also improved. The results indicate that the 1/*f* noise and other even low frequency interferences, such as electronic interference in the feedback path of the closed loop, is alleviated by MFA.

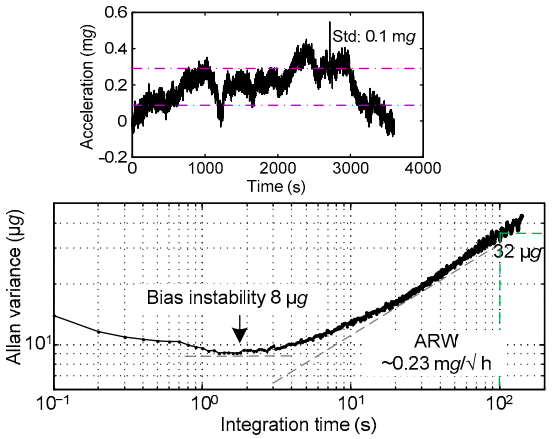

Fig. 14 One-hour stability test with zero acceleration input by applying a modulated feedback approach
The large plot shows the Allan variance results and the inset is the time-domain trace

3.2 Temperature compensation experiments

After realizing the modulated feedback approach, we continue to construct the compensation experiments based on MFA. The temperature experiments are set up in a temperature chamber. The photographs are displayed in Fig. 15.

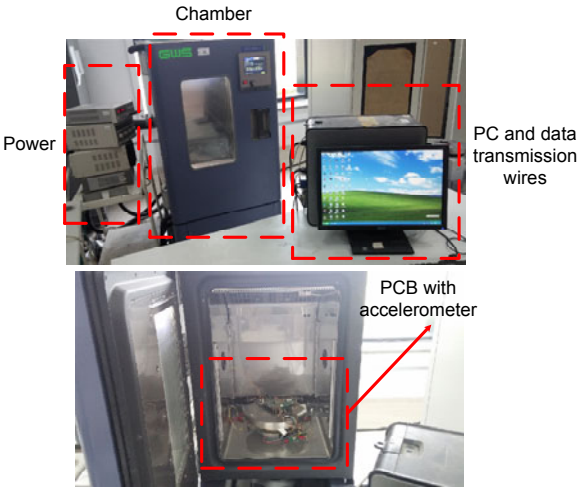

Fig. 15 Photographs of the temperature experiment setup
The PCB and FPGA are mounted on the rate table in the temperature chamber

V_{pid} and V_{ref} are measured from 10 °C to 50 °C with a 5 °C interval in the temperature compensation experiment. We set the stable PID output at 30 °C as the zero acceleration output. The measured results are shown in Fig. 16. The line with square label is the V_{pid} output, and the line with triangle label is the V_{ref} output. Both lines show high linearity with temperature. The 1st order fitted result of V_{pid} is y=4.685T−145.739, where T is the temperature. This means that the temperature coefficient of V_{pid} is about 4.68 mg/°C. The first-order fitted result of V_{ref} is y=−0.008T+43.731. Since the phase linearly changes with temperature, the compensation is valid by using V_{ref} to indicate the temperature variation. Hence, we implement the first compensation algorithm: using V_{ref} to compensate for the V_{pid}. The compensation results are given as the line with circle label in Fig. 16. The first-order fitted result of compensated output is y=0.1T−3.834, which means that the temperature coefficient has been decreased to 0.1 mg/°C. There is a 46 times improvement on the temperature coefficient.

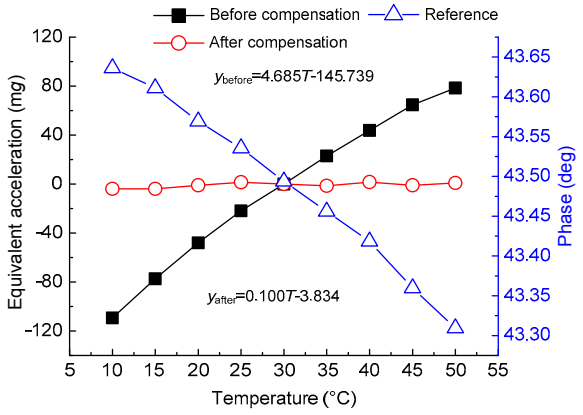

Fig. 16 Measured closed-loop output before and after compensation

The reference signal V_{ref} is also added. The closed-loop output and the reference signal both vary linearly with temperature, making the compensation easy to realize with the first-order compensation algorithm

In addition to the static temperature experiments, the closed-loop system may suffer from a harsh environment like fast temperature variation and requires immediate response to environment changes. Therefore, we explore the capability of the compensation approach when confronting large temperature change in a short time. Fig. 17 presents the online compensation block input and output when suffering from the impact of an additional cooling device. The three signals are stable before the cooling device starts to work at 70 s. Then the cooling device starts, and the signals V_{pid} and V_{ref} show large drift and their drift directions are opposite. During the 120 s cooling process, the temperature roughly changes by about 3 °C, and V_{pid} has drifted by about 8 mg, but the compensated signal V_{out} shows much smaller variation as indicated by the insert of Fig. 17. After the cooling process stops, the temperature rises to the origin level, so do the signals V_{pid} and V_{ref}. During the whole process, the largest drift for V_{out} is 1 mg, which may result from the temperature lag effect of the accelerometer and circuits. Hence, this experiment suggests that online compensation can still achieve a relatively desirable result under a fast environment variation.

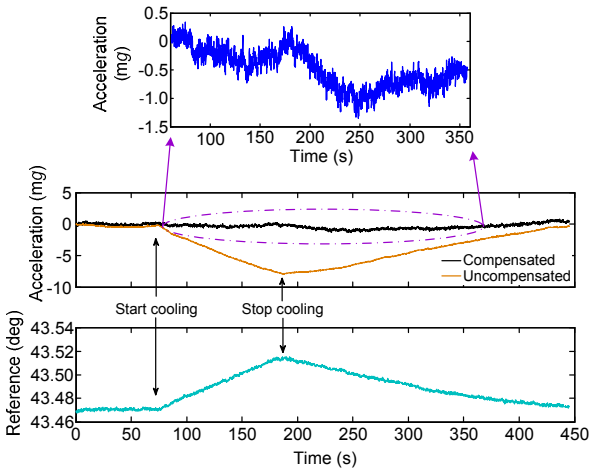

Fig. 17 Online compensation results under a fast temperature variation generated by the cooling device

The 1.5 h zero acceleration input tests are conducted for three runs with different accelerometers, and the corresponding Allan variance results are shown in Fig. 18. Each run of the stability test is conducted on different days. The black solid line has the largest bias instability and the long-term drift, and we adopt this line for further analysis in Fig. 19.

The time-domain trace of the black solid line in Fig. 19 achieves a standard deviation of about 0.079 mg, smaller than the trace with only MFA. However, the bias instability increases to 13 μg.

Since the compensation algorithm is using V_{ref} to linearly compensate for the V_{pid}, the increase of bias instability is quite likely to come from the noise of V_{ref}.

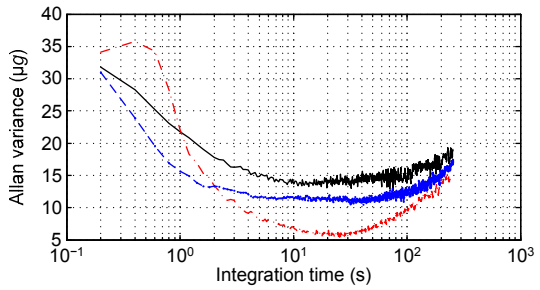

Fig. 18 Results of three runs of Allan variance of the temperature compensated closed-loop output
Each run is conducted with an interval of more than three days at room temperature and with different accelerometers, whose resonant frequencies are around 800 Hz

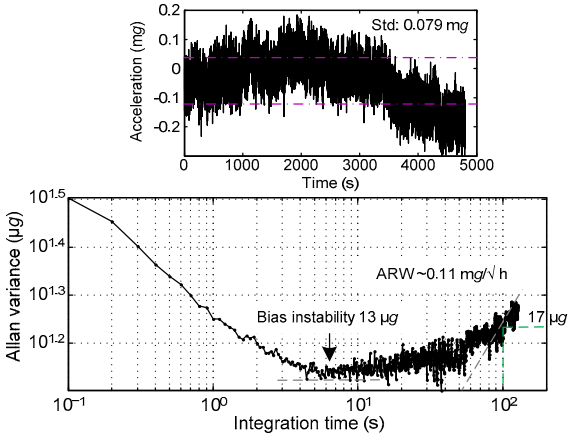

Fig. 19 Online compensation time-domain trace and the Allan variance results demonstrated by the black solid line in Fig. 17

Theoretically, as the residual 1/*f* noises in the feedback path and forward path are directly applied on the variable capacitors, the capacitance gap will be affected by the 1/*f* noise voltage. According to Eq. (24), parameter d_0 is the capacitance gap which introduces the 1/*f* noise. Therefore, V_{ref} in Eq. (24) which contains d_0 will also exhibit the characteristic of 1/*f* noise.

The V_{ref} is sampled to verify such a theory. The noise level of V_{ref} after Allan variance calculation is 1.7 μg, and the noise power spectral density is 0.3 μg at 0.1 Hz and 2 μg at 0.01 Hz after fast Fourier transform (FFT), showing the 1/*f* noise shape in the FFT plot. The results suggest that the 1/*f* noise in V_{ref} causes performance degradation.

However, compared with the value of 32 μg obtained using MFA only, the long-term drift is improved to around 17 μg at 100 s of the integration time (Fig. 19). Moreover, results of three runs of Allan variance in Fig. 18 have almost the same values of drift at 100 s of the integration time. This indicates that temperature compensation is especially useful for the improvement of long-term drift whose period is longer than that of bias instability.

4 Discussion

Based on the experiments in Section 3, the test results of open loop, closed loop with DFA, closed loop with MFA, and closed loop with MFA and temperature compensation are all listed in Table 3 for clear comparison.

From the aspect of time-domain trace Std, the drift is indeed improved, from 0.52 to 0.079 mg.

As for bias instability, the 1/*f* noise in the feedback path deteriorates the performance and the closed-loop results with DFA are worse than the open-loop results. The closed loop with MFA minimizes the 1/*f* noise and achieves similar bias instability results to the open loop. The closed loop with MFA and temperature compensation slightly degrades the bias instability, mainly due to the 1/*f* noise in V_{ref}.

For the long-term drift at 100 s of the integration time, the open loop has the largest drift while the closed loop with MFA and temperature compensation has the smallest value. This is similar to the comparison result of time-domain trace Std.

Taking account of the temperature coefficient, the closed loop with MFA and temperature compensation has an improvement 46 times that of the closed loop with MFA. Its temperature coefficient reaches as little as 0.1 mg/°C.

The comparison in Table 3 indicates that MFA is useful for minimizing the 1/*f* noise in the feedback path. The temperature compensation helps alleviate the long-term drift, whose period is longer than that of bias instability in the Allan variance plot. The combined approach of these two methods can indeed improve the overall bias performance of the closed-loop accelerometer.

Table 3 Time-domain and Allan variance performance comparison

Mode	Time-domain trace Std (mg)	Bias instability (μg)	Drift at 100 s of integration time (μg)	Temperature coefficient (mg/°C)
Open loop	0.520	12	180	−
Direct feedback	0.350	32	72	>4.685
Modulated feedback	0.100	8	32	4.685
Modulated feedback with temperature compensation	0.079	<13	<17	0.100

5 Conclusions

We demonstrate a novel combined approach to improve the bias drift of a closed-loop MEMS accelerometer. The modulated feedback approach is first used to isolate the 1/*f* noise existing in a conventional direct feedback approach. Based on the modulated feedback approach, a common mode signal reflecting the temperature drift of circuits is added to the closed loop. The phase of the signal is measured linearly with temperature and can be used for compensation. The online compensation achieves a temperature coefficient of 0.1 mg/°C in the temperature range of 10−50 °C, and can effectively minimize the impact of fast temperature variation in a closed-loop system. The bias instability increases slightly to 13 μ*g* and the bias drift decreases to 17 μ*g* with the combined approach at 100 s of the integration time. Such a combined approach uses the potential of a closed loop and can be useful for other accelerometer systems.

Acknowledgements

The authors would like to thank Zhe LI and Xian-ge HE with the Micro-Satellite Research Center, Zhejiang University for their kind assistance and advice on this work.

References

Aaltonen, L., Halonen, K., 2009. Continuous-time interface for a micromachined capacitive accelerometer with NEA of 4 μg and bandwidth of 300 Hz. *Sens. Actuat. A*, **154**(1):46-56. [doi:10.1016/j.sna.2009.07.011]

Allan, D.W., 1966. Statistics of atomic frequency standards. *Proc. IEEE*, **54**(2):221-230. [doi:10.1109/PROC.1966.4634]

Amini, B.V., Abdolvand, R., Ayazi, F., 2006. A 4.5-mW closed-loop ΔΣ micro-gravity CMOS SOI accelerometer. *IEEE J. Sol.-State Circ.*, **41**(12):2983-2991. [doi:10.1109/JSSC.2006.884864]

Chae, J., Kulah, H., Najafi, K., 2005. A CMOS-compatible high aspect ratio silicon-on-glass in-plane micro-accelerometer. *J. Micromech. Microeng.*, **15**(2):336-345. [doi:10.1088/0960-1317/15/2/013]

Cui, J., Guo, Z.Y., Yang, Z.C., *et al.*, 2011. Electrical coupling suppression and transient response improvement for a microgyroscope using ascending frequency drive with a 2-DOF PID controller. *J. Micromech. Microeng.*, **21**(9):1-11. [doi:10.1088/0960-1317/21/9/095020]

Dong, Y., Kraft, M., Redman-White, W., 2007. Higher order noise-shaping filters for high-performance micromachined accelerometers. *IEEE Trans. Instrum. Meas.*, **56**(5):1666-1674. [doi:10.1109/TIM.2007.904477]

Dong, Y., Zwahlen, P., Nguyen, A.M., *et al.*, 2010. High performance inertial navigation grade sigma-delta MEMS accelerometer. Proc. IEEE/ION Position Location and Navigation Symp., p.32-36. [doi:10.1109/PLANS.2010.5507135]

Enz, C.C., Temes, G.C., 1996. Circuit techniques for reducing the effects of OP-AMP imperfections: autozeroing, correlated double sampling, and chopper stabilization. *Proc. IEEE*, **84**(11):1584-1614. [doi:10.1109/5.542410]

IEEE, 1998. IEEE Standard Specification Format Guide and Test Procedure for Single-Axis Interferometric Fiber Optic Gyros. IEEE Std 952-1997. [doi:10.1109/IEEESTD.1998.86153]

Josselin, V., Touboul, P., Kielbasa, R., 1999. Capacitive detection scheme for space accelerometer applications. *Sens. Actuat. A*, **78**(2-3):92-98. [doi:10.1016/S0924-4247(99)00227-7]

Kajita, T., Moon, U.K., Temes, G.C., 2002. A two-chip interface for a MEMS accelerometer. *IEEE Trans. Instrum. Meas.*, **51**(4):853-858. [doi:10.1109/TIM.2002.803508]

Karabalin, R.B., Villanueva, L.G., Matheny, M.H., *et al.*, 2012. Stress-induced variation in the stiffness of micro- and nanocantilever beams. *Phys. Rev. Lett.*, **108**:236101. [doi:10.1103/PhysRevLett.108.236101]

Ko, H., Cho, D.D., 2010. Highly programmable temperature compensated readout circuit for capacitive microaccelerometer. *Sens. Actuat. A*, **158**(1):72-83. [doi:10.1016/j.sna.2009.12.017]

Lakdawala, H., Fedder, G.K., 2004. Temperature stabilization of CMOS capacitive accelerometers. *J. Micromech. Microeng.*, **14**(4):559-566. [doi:10.1088/0960-1317/14/4/017]

Lee, J., Rhim, J., 2012. Temperature compensation method for the resonant frequency of a differential vibrating accelerometer using electrostatic stiffness control. *J.*

Micromech. Microeng., **22**(9):1-11. [doi:10.1088/0960-1317/22/9/095016]

Lee, K., Takao, H., Sawada, K., *et al.*, 2003. A three-axis accelerometer for high temperatures with low temperature dependence using a constant temperature control of SOI piezoresistors. Proc. 16th IEEE Annual Int. Conf. on Micro Electro Mechanical Systems, p.478-481. [doi:10.1109/MEMSYS.2003.1189790]

Li, M., Horsley, D.A., 2014. Offset suppression in a micromachined Lorentz force magnetic sensor by current chopping. *J. Microelectromech. Syst.*, **23**(6):1477-1484. [doi:10.1109/JMEMS.2014.2316452]

Liu, D., Chi, X., Cui, J., *et al*., 2008. Research on temperature dependent characteristics and compensation methods for digital gyroscope. Proc. 3rd Int. Conf. on Sensing Technology, p.273-277. [doi:10.1109/ICSENST.2008.4757112]

Petkov, V.P., Boser, B.E., 2004. Capacitive interfaces for MEMS. *In*: Baltes, H., Brand, O., Fedder, G.K., *et al.* (Eds.), Enabling Technology for MEMS and Nanodevices. Wiley-VCH Weinheim, p.49-92. [doi:10.1002/9783527616701.ch3]

Prikhodko, I.P., Trusov, A.A., Shkel, A.M., 2013. Compensation of drifts in high-*Q* MEMS gyroscopes using temperature self-sensing. *Sens. Actuat. A*, **201**:517-524. [doi:10.1016/j.sna.2012.12.024]

Samarao, A.K., Ayazi, F., 2012. Temperature compensation of silicon resonators via degenerate doping. *IEEE Trans. Electron Dev.*, **5**9(1):87-93. [doi:10.1109/TED.2011.2172613]

Schreier, R., 1993. An empirical study of high-order single-bit delta-sigma modulators. *IEEE Trans. Circ. Syst. II*, **40**(8):461-466. [doi:10.1109/82.242348]

Willemenot, E., Touboul, P., 2000. On-ground investigation of space accelerometer noise with an electrostatic torsion pendulum. *Rev. Sci. Instrum.*, **71**(1):302-309. [doi:10.1063/1.1150197]

Wongkomet, N., Boser, B.E., 1998. Correlated double sampling in capacitive position sensing circuits for micromachined applications. Proc. IEEE Asia-Pacific Conf. on Circuits and Systems, p.723-726. [doi:10.1109/APCCAS.1998.743923]

Wortman, J.J., Evans, R.A., 1965. Young's modulus, shear modulus, and Poisson's ratio in silicon and germanium. *J. Appl. Phys.*, **36**(1):153-156. [doi:10.1063/1.1713863]

Wu, J., Fedder, G.K., Carley, L.R., 2004. A low-noise low-offset capacitive sensing amplifier for a 50-μg/√Hz monolithic CMOS MEMS accelerometer. *IEEE J. Sol.-State Circ.*, **39**(5):722-730. [doi:10.1109/JSSC.2004.826329]

Yoshida, Y., Kakuma, H., Asanuma, H., *et al*., 2005. A linear model based noise evaluation of a capacitive servo-accelerometer fabricated by MEMS. *IEICE Electron. Expr.*, **2**(6):198-204. [doi:10.1587/elex.2.198]

Zheng, X., Jin, Z., Wang, Y., *et al.*, 2009. An in-plane low-noise accelerometer fabricated with an improved process flow. *J. Zhejiang Univ.-Sci. A*, **10**(10):1413-1420. [doi:10.1631/jzus.A0820757]